

Construction and Analysis of a Lightweight UAV Wing Prototype

Mário Hernâni Silva Ramos
mario.ramos@ist.utl.pt

Instituto Superior Técnico, Lisboa, Portugal

November 2015

Abstract

An increase in the usage of Unmanned Aerial Vehicles (UAV) in recent years has led to a more competitive market where more attention is being given to efficiency and safety. Bearing that in mind, a greater focus is put on their preliminary structural design, where the development of computational Finite Element Analysis (FEA) methods allow for a better prediction of the behavior of the final structure. In this work, a prototype based on a new, suggested wing structure for a particular fixed wing UAV is built, and the results obtained by experimental tests are compared to those yielded by a numerical model developed in CATIA[®]. To do so, a CAD model of both the suggested wing structure and its prototype is created, based on identified design parameters. The materials selected for the prototype are tested, their elastic properties determined and a validation of those tests made in CATIA[®]'s Generative Structural Analysis workbench. The building process of the prototype is described, and considerations regarding the influence of each material and part in its final weight are made. The tests performed on the prototype are presented, and a comparison between their results and those of the FEA is made, followed by a discussion of the differences between them. Conclusions on the accuracy of the numerical model are drawn, and suggestions of ways to minimize those discrepancies by means of a more controlled building process are presented. This effort is aimed to pave the way for future higher-fidelity computational structural designs of UAVs using the tuned FEA tools.

Keywords: Finite element method, Material properties, Materials testing, Validation, Prototype, Structural analysis.

1. Introduction

Nowadays, we are witnessing an increase in the usage of Unmanned Aerial Vehicles (UAVs), also known as drones or Remotely Piloted Aircraft Systems (RPAS) not only for the more traditional military operations, but also for civilian purposes. Given this growth in the market of UAVs, it is of a great importance to be able to design and build vehicles that are suited for the mission at hand, being able to complete such mission in the safest and most efficient manner possible. As such, it is necessary to consider all factors that influence the performance of the UAV as early in the design process as possible. The significant evolution of computers over the last few decades has allowed for an easier design of such structures. Existing commercial structural analysis software packages using Finite Element Methods (FEM) give the opportunity for the designers to simulate the behavior of the structures even before a physical prototype is built. It is, however, very important for the designers to obtain a model as faithful as possible to its future real life counterpart. This thesis is focused on obtaining a numerical model that can be put to use in a

preliminary design phase of a new wing structure for a Long Endurance Electric UAV (LEEUAV) for civilian surveillance missions. The UAV has been developed as a product of the LEEUAV project [1], and already has a fully functional wing. A new wing structure will be proposed based on that existing one, with slight modifications that may allow for a better behavior and reduced weight. A prototype of that structure will be built, and static tests performed on it. The results will then be compared with those yielded by the numerical model of that prototype, and conclusions regarding its accuracy were drawn. The materials used on the wing will be tested and their properties determined prior to the structural analysis of the prototype. A fine tuning of the numerical model will be performed based on a validation of those properties using the same FEM software to be used to perform the structural analysis, to obtain a numerical model as faithful to reality as possible.

2. Background

Before performing any task, an identification of the structural and aerodynamic characteristics of the existing UAV was made.

2.1. General UAV Characteristics

The general LEEUAV characteristics identified in [1] need to be considered before performing future tasks. The main specifications that drove the design of the UAV were long endurance, usage of green power sources, ability to fly autonomously and usage of a high-strength and lightweight structure, built with composite materials. Its mission profile consists of a very short takeoff distance, which should happen in 8 meters for the case of an autonomous takeoff or in 3 meters in case of it being hand launched. The UAV should then climb to its cruise altitude of 1000 meters in 10 minutes, where it should fly for 8 hours at a speed above a threshold of 7 m/s. Following the cruise section of its mission, the UAV should be able to descend without power for 29 minutes and land. The desired performance parameters are presented in Table 1

Cruise speed [m/s]	7.5
Maximum climb rate [m/s]	2.2
Lift-to-drag ratio	20
Maximum speed [m/s]	21.1
Stall speed [m/s]	6.1
Takeoff roll distance [m]	8.1

Table 1: Desired UAV performance.

A new airfoil was designed in order to meet the requirements set for the UAV. The wing built was comprised of three different sections, with a 13.5 aspect ratio, 4.50 m span and a total wing area of 1.518 m^2 . The main LEEUAV characteristics may be found in Table 2. Figure 1 shows the current LEEUAV in flight.

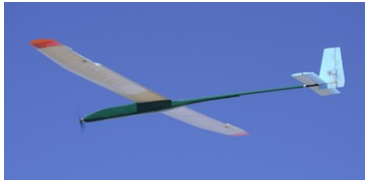


Figure 1: Current LEEUAV.

A hybrid system comprised of batteries and solar panels was chosen to power an electric motor. An open source autopilot system was also implemented.

2.2. Aerodynamic Loads

Based on the work carried out in [2], an estimation of the aerodynamic forces acting on the existing wing was made. Using FreeCAD[®], the author of [2] created a CAD model of the UAV, and performed a CFD analysis of it. Star-CCM+[®] was the software package chosen to perform the analysis. After a validation process, $k-\omega$ SST turbulence model [3], together with $\gamma - Re_\theta$ transition model [4] were determined to yield better results than the

Span [m]	4.500
Length [m]	2.370
Root wing chord [m]	0.350
Tip wing chord [m]	0.250
Wing area [m^2]	1.518
Aspect ratio	13.500
Tailplane chord [m]	0.213
Tailplane span [m]	0.850
Tailplane area [m^2]	0.181
Root empennage chord [m]	0.258
Tip empennage chord [m]	0.364
Empennage area [m^2]	0.077
Structure mass [Kg]	1.590
Empty mass [Kg]	3.890
Takeoff mass [Kg]	4.900

Table 2: Main LEEUAV characteristics.

Spalart-Allmaras turbulence model [5], predicting accurately the aerodynamic coefficients, as well as the location at which natural transition occurred. Using those models, for an angle of attack of 0 and the reference values summarized in Table 4, the aerodynamic performance parameters of the UAV presented on Table 3 were determined.

$C_{L_{max}}$	1.51
$\alpha_{C_{L_{max}}}$	8
α_{lift}	-9.5
C_{L_α}	$5.59 rad^{-1}$
$C_{D_{min}}$	0.0527
$C_{D,0}$	0.06
$(C_L/C_D)_{max}$	14.01
$\alpha_{C_L/C_D)_{max}}$	0
$(C_L^{3/2}/C_D)_{max}$	15.06
$\alpha_{(C_L^{3/2}/C_D)_{max}}$	2

Table 3: UAV performance parameters.

Reference density	$1.184 Kg/m^3$
Reference pressure	0 Pa
Reference velocity	7.48 m/s
Reference area	$0.781 m^2$

Table 4: Reference values used in CFD analysis.

Performing a post processing operation on the results, the pressure distribution along the wing was obtained in two different manners. Since it would be impossible to process that data in the whole wing in a continuous manner, both along the span and the chord, a discrete approach was taken along one of these dimensions. In a first approach, thirteen derived parts were defined at different points along the wingspan. These parts consisted of 2 cm wide slices of the wing surface, where the pressure coefficient was measured. The spacing between these sections

was gradually decreasing, from the wing root to the tip, as it is expected that the pressure coefficient will vary more near the wing tip. In a second approach, a total of eight derived parts similar to the previously described, also 2 cm wide, were defined at different points of the wing chord, allowing for a continuous measurement of the pressure coefficient along the span. These were homogeneously spaced. Both approaches are schematically presented in Figure 2, showing a planform view of the left wing.

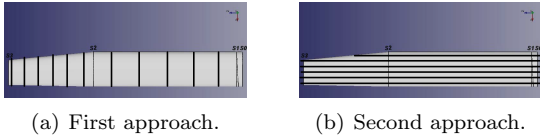


Figure 2: Approaches used for the estimation of the aerodynamic loads.

The data was then exported from Star-CCM+[®], imported into a spreadsheet table, and plotted to obtain the pressure coefficient distribution for each of the mentioned derived parts. Figure 3 shows a plot of the pressure coefficient data for a slice between 1.1 and 1.2 m along the chordwise position. A similar graph was obtained for each of the data sets gathered by both approaches. These pressure coefficient distributions allow for the determination of the forces acting on the wing structure.

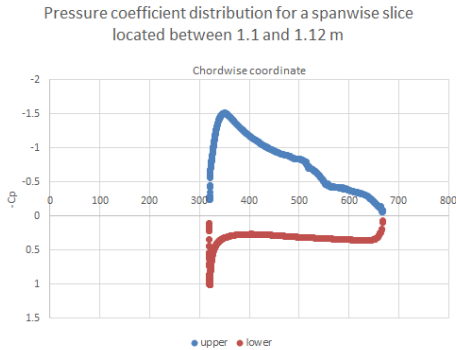


Figure 3: Pressure coefficient distribution for a chordwise slice between 1.1 and 1.12 m.

2.3. Existing Wing Structure

A D-box type structure was chosen for the wing. This box consists of two pultruded carbon spar caps and a 0.15 mm thick carbon fiber reinforce plastic (CFRP) skin, wrapped around a low density foam core. Plywood was used to build the strong aft ribs, while the light ones were built using balsa wood, as well as the trailing edge stringer. These structural features can be seen in Figure 4 (a). The entire wing is covered by a thin sheet of heat-shrinking material.

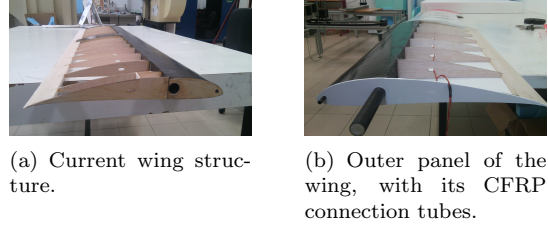


Figure 4: Current wing features.

This wing is divided into three different sections that can be disassembled for transportation, one central panel with 12 solar cells and two outer panels, consisting of a rectangular zone containing the remainder of the solar cells and the tapered zone of the wing, where the ailerons are placed. Two CFRP tubes are responsible for the transfer of bending moments from the outer panels to the central panel of the wing, and can be seen in Figures 4 (a) and (b).

2.4. Wing Design

When designing a new wing for an aircraft, one first needs to take into account the aerodynamic aspects of the wing. The several steps outlined in [6] for a wing design were presented.

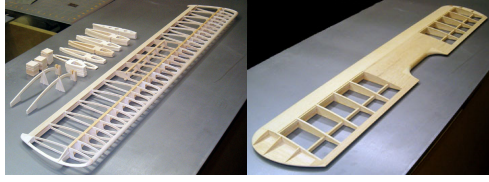
Since the LEEUAV is fundamentally an aircraft model, the types of wing structures usually used in that type of aircraft were identified. The non-sheeted rib and spar construction, which can be observed in Figure 5 (a), simply consists of a spar with ribs whose shape matches the designed airfoil. Most of the structure itself is hollow, which makes for an incredibly lightweight, yet flexible, wing.

The semi-sheeted wing, presented in Figure 5 (b) differs from the previously presented structure in the fact that it possesses a sheeted section, with the shape of the airfoil. The D-box wing structure is an example of a semi-sheeted wing. It is sheeted from the main spar to the leading edge, providing the D shape that names it. The inside of the sheeted area, the D-box, can be either hollow or filled with some sort of material, such as foam. This wing structure is heavier than the non-sheeted rib and spar construction, but the added stiffness allows the wing to support higher loads.

A type of structure also considered was the fully-sheeted wing, shown in Figure 5 (c). This type of wing may have a regular rib and spar inner structure, or a foam core, being heavier than both previous structures. However, it does not bring significant improvements to the wing structural behavior.

3. Wing Model

A description of the creation of the CAD model of the wing was made, as independently from a specific wing structure design as possible.



(a) Non-sheeted rib and spar construction. (b) D-box semi-sheeted wing.



(c) Fully-sheeted wing.

Figure 5: Wing structures used in model aircraft

3.1. Identification of Design Parameters

Since a parametric design process allows for a swift adjustment of the CAD model, without the need to start the whole process over and over again, the main design parameters were identified. Since the aerodynamic properties of the existing wing are to be kept, the airfoil used in the CAD models will be the one developed for the LEEUAV in [1], being the overall wing configuration of the existing wing kept. As such, the wingspan, chord, and other geometric features of the wing presented in Table 2 were used.

By looking at the different types of structures considered, one may identify that they share several common features, such as ribs, and a spar (whose cross-section may vary). A circular boom was also considered for adding stiffness to the wing. Several parameters concerning these parts and their relative positions were identified, as presented in Table 5. Since no dihedral angle is to be applied, only the wing incidence angle was relevant in order to obtain the desired washout angle at the wing tip.

3.2. CAD Modeling Process

After a software selection process which resulted in CATIA[®] being chosen for its user friendly interface and incorporated structural analysis workbench, a generic parametric CAD modeling process to obtain the left half-wing was described, taking into account the parameters presented in Table 5.

The airfoil profile was drawn in CATIA[®], and the overall shape of the ribs obtained. The wing has a constant chord until 1400 mm span. After this point, the chord decreases linearly, from 350 mm on the previous section of the wing to 250 mm measured at the wing tip, and the incidence angle varies from 0 at 1400 mm to 4.5 degrees at the wing tip. Scaling and rotation operations were performed to obtain the ribs in that region.

The spar and circular boom were modeled next,

Parameter description	Parameter symbol
Half wing span	b
Root chord	c_r
Tip chord	c_t
Rib spacing	r_s
Rib thickness	r_t
Rib hollowness	r_h
Web length	W_l
Web thickness	W_t
Top flange length	TF_l
Top flange thickness	TF_t
Bottom flange length	BF_l
Bottom flange thickness	BF_t
Spar chordwise position	S_{cp}
Circular boom outer diameter	d_o
Circular boom inner diameter	d_i
Circular boom chordwise position	B_{cp}
Incidence angle of the wing	iW

Table 5: Wing parameters.

and their cross-sections cut on the rib shapes previously obtained. An aileron was obtained, and a generic non-sheeted structure assembled.

4. Structural Analysis

4.1. FEM Applied to a Wing

Since the fundamentals of the FEM presented in [7] apply regardless of the problem under consideration, attention was given to the options provided by CATIA[®]'s Generative Structural Analysis workbench.

The two types of tetrahedron elements available in CATIA[®] were identified, and their properties outlined. The tetrahedral linear element, with its four nodes was found to be susceptible to producing less accurate results, while the tetrahedral quadratic element, having six more nodes and using quadratic interpolation functions, yielded more accurate results at the cost of additional computational resources.

The mesh parameters were identified, and it was seen that the sag parameter, determining how well the finite elements mesh matches the geometry of a part, had a significant influence on the obtained mesh.

After selecting the type of element used for the simulation, as well as providing a first value for the mesh parameters, it was necessary to define the type of interaction between each part of the assembly. Three different types of connection properties were tested.

The rigid connection property links two bod-

ies which are fastened together at their common boundaries. What it does is to create a rigid spider finite element which connects all the nodes of the interacting surfaces to a null-length bar created at the midpoint between the nodes of the two meshed parts. This type of connection does not take into account the elastic deformation between the interface surfaces, considering it to be infinitely rigid, thus not appropriate for this case. The smooth connection is similar to the rigid one, in the sense that it is used to link two bodies which are fastened together using a spider. However, it takes into account an approximate elastic deformability of the interface between the bodies. The fastened connection simply merges the nodes of the meshes of the interacting surfaces. By doing so, more than taking into account the elastic deformation of the interface between the bodies, they act as if they become a single body. It was found that the fastened connection described more accurately the real life problem, and so it was selected.

As for the boundary conditions, according to the wing design methodology presented in [6], it was assumed that the spar and the stiffening circular beam are cantilever beams, fixed at their roots.

4.2. Validation

After presenting the constitutive laws for the several types of materials used in the wing model, a simple validation problem was carried out, considering a cantilever beam with a rectangular cross section, loaded at its free end, made of an isotropic material, in this case Titanium, whose elastic properties are summarized in Table 6. The problem is depicted in Figure 6. A force of $P=50$ N was considered, applied downwards at the free end.

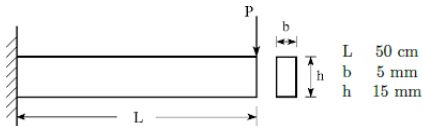


Figure 6: Cantilever beam validation problem.

E	$1.14 \cdot 10^{11}$ Pa
ν	0.34
ρ	4460 Kg/m^3
σ_{yield}	$8.25 \cdot 10^8$ Pa

Table 6: Material properties of the titanium used on the beam.

After a convergence study was carried out, a mesh with 28069 quadratic tetrahedron elements was chosen, and the results of the FEA compared with the theoretical ones [8], given by

$$y = \frac{Px^2}{6EI}(3L - x), \quad (1)$$

where E is the Young's modulus of the material and I the area moment of inertia of the beam cross-section (considering y to be the vertical axis, and x the axis along the beam length, l).

A perfect match of the results was found, with a displacement of the free end of 13 mm obtained by both the FEA, as shown in Figure 7, and theoretical results. It was concluded that CATIA®'s Generative Structural Analysis workbench is capable of producing results with an extremely good accuracy, given that the appropriate options are used.

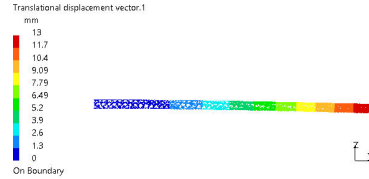


Figure 7: Deformed shape of the beam.

5. Materials Study

In order to determine the properties of the materials used on the wing prototype, they had to first be identified. Table 7 summarizes the materials selected and the parts for which they were considered

Material	Part
Balsa wood	Spar and ribs
Plywood	Ribs
Pultruded carbon tube	Boom
Fiberglass composite	Spar and ribs reinforcement
Heat shrink plastic	Cover

Table 7: Materials considered for building the prototype.

5.1. Wood Testing Procedure

After analyzing the recommendations of ASTM Standard D143-94 [9], and considering the limitations imposed by the available sources of balsa wood, it was determined that only the tension parallel to the grain tension test could be performed. Since wood is an orthotropic material, the elastic properties in the remaining directions were estimated based in the relations presented in [10] and the results of that tension parallel to the grain tension test.

Using a CNC milling machine, a specimen based on the one recommended in [9] was cut, and can be seen in Figure 8 (a). Since the grips recommended in those standards were not available, modifications were made to the specimen. The active test region, however, was kept in accordance to the ASTM

standards. A 10 kN loading cell was mounted on the Instron[®] 5566 electromechanical tension testing machine, and a Instron[®] uniaxial extensometer (CAT N 2620-602) used to measure the deformation of the specimen. Figure 8 (b) illustrates the test setup used.



(a) Specimen. (b) Test setup.

Figure 8: Parallel to the grain tension test

Using the data gathered during the test, it was possible to plot a stress versus strain graph of the linear region, illustrated in Figure 9, where the specimen was assumed to have an elastic behavior on the region of the extensometer, and a value of 2.65 GPa extracted from the trend line equation

$$\sigma = 2.65 \cdot 10^9 \epsilon - 3.37 \cdot 10^5. \quad (2)$$

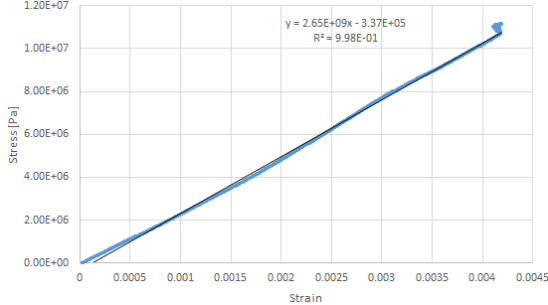


Figure 9: Stress with respect to strain plot for the balsa tension parallel to grain test (second specimen).

Based on that value and the relation between elastic properties presented in [10], the elastic properties for balsa wood were determined, and are summarized in Table 8.

5.2. Carbon Tube Testing Procedure

The pultruded carbon tube, with an outer and inner diameters of 4 and 3 mm respectively, was assumed to be isotropic, and a simple bending test performed. A support was built, already accounting for the fixation of the wing prototype at a later stage, and different masses applied at the free end of the tube, considering two different spans. The displacements were measured, and, using Equation

Young's Modulus		Poisson's Ratio	
E_L	2,650 MPa	μ_{LR}	0.229
E_T	39.75 MPa	μ_{LT}	0.488
E_R	121.90 MPa	μ_{RT}	0.665
G_{LR}	143.10 MPa	μ_{TR}	0.231
G_{LT}	98.05 MPa	μ_{RL}	0.018
G_{RT}	13.25 MPa	μ_{TL}	0.009

Table 8: Elastic properties of the tested balsa wood.

(1), it was possible to determine the Young's modulus for each load/span combination, shown in Table 9. An average value of 108.18 GPa was determined, presenting a 15.5% discrepancy relatively to the 125 GPa presented by most manufacturers.

Load [gf]	E [GPa] (360 mm span)	E [GPa] (500 mm span)
133.47	102.96	108.64
266.74	106.35	113.72
621.79	109.23	—

Table 9: Young's Modulus determined for each span/loading combination.

5.3. Composite Testing Procedure

Based on ASTM Standard D3039 [11], a tension test was carried out on a single layer fiberglass composite specimen, with a length of 100 mm, a width of 20 mm and a rectangular cross section with a measured thickness of 0.10 mm. In this specific case, the fibers used came in the form of a fabric, where two directions of fiber orientation can be identified, perpendicular to each other. Since a tension test was performed, these fibers were oriented in the directions parallel and perpendicular to the loading. By doing so, when obtaining the Young's Modulus for the direction parallel to the loading, the one in the direction perpendicular to it is known to be equal.

The same tension testing machine and extensometer employed for the wood tests were used. Using the data gathered during the test, a stress versus strain plot of the elastic region was obtained and is presented in Figure 10, and based on the trend line equation

$$\sigma = 7.35 \cdot 10^9 + 3.42 \cdot 10^5. \quad (3)$$

a value of 7.35 GPa was determined for the Young's modulus in the two aforementioned directions.

6. Validation of the Numerical Models

Validation of the tests was then carried out using CATIA[®]'s Generative Structural Analysis workbench. The tests were modeled and solved numerically, using the previously determined properties,

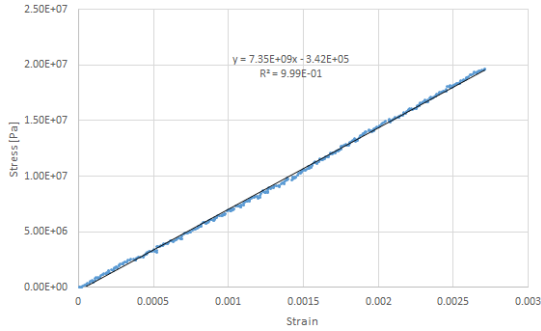


Figure 10: Stress vs. strain plot of the elastic region (composite specimen).

and the results compared with the experimental ones to assess if there was a need to tune the material properties.

6.1. Balsa Wood Model

The central region of the wood specimen was modeled, and the experimentally determined material properties assigned to it taking into account the orientation of the fibers. One end was clamped, while on the surface of the other a uniformly distributed force of 200.08 N was applied. A maximum displacement of 0.116 mm was expected, based on the experimental data.

A convergence study was carried out, and a mesh with a total of 47363 elements selected. This mesh was obtained with a global element size of 0.75 mm, and a local refinement in the region where the force was applied using elements with 0.15 mm. Figure 11 shows the obtained displacement results using that mesh. A value of 0.116 mm is obtained for the maximum displacement, meaning that a perfect match with the experimental results was obtained.

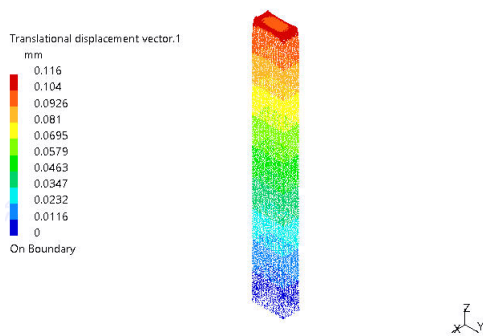


Figure 11: Deformation of the specimen under the selected loading.

6.2. Carbon Tube Model

To minimize the error of the analysis, the span/loading pair which yielded the value of the Young's modulus closest to the final average of 108.18 GPa was chosen. As such, a tube with a

length of 500 mm was modeled, one of its ends clamped and a load of $0.13347 \cdot 9.81 = 1.309$ N applied on the other, perpendicular to its axis. After performing a convergence study, a mesh with 134774 quadratic tetrahedron elements was chosen, and a displacement of 58.6 mm obtained at the free end, as seen in Figure 12. A discrepancy of 0.34% is obtained when considering the experimental result of a 58.4 mm maximum displacement, meaning that no tuning of the elastic properties of the material was necessary.

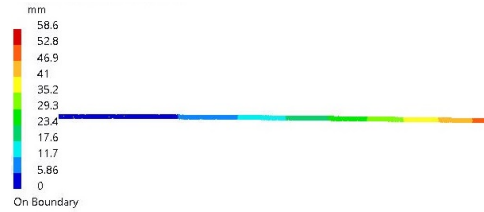


Figure 12: Deformed shape of the carbon tube.

6.3. Fiberglass Composite Model

Due to the extremely reduce thickness of the specimen, validation was first performed using a 2D mesh, with 500 quadrangular elements, and assuming isotropic properties, based on the assumption that, given the fact that the fibers were woven perpendicularly, the elastic properties in the two directions can be considered equal. This mesh was selected in the wake of a convergence study. Considering a force of 20 N, applied on the free end, a maximum displacement of 0.142 mm was obtained, as seen in Figure 13. This constitutes a relative difference of 3.40%, compared to the experimental results of 0.147 mm.

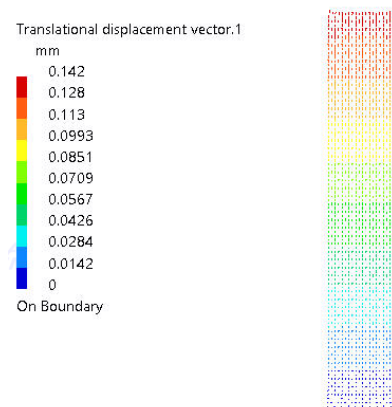


Figure 13: Deformed shape of the composite specimen (2D mesh 2).

Validation was then performed considering a 3D mesh, and isotropic behavior. After a convergence

study was undertaken, a mesh with 47919 quadratic tetrahedron elements was chosen, and, for the same applied load of 20 N, a maximum displacement of 0.139 mm was obtained. A relative error of 5.44% is present. Since this error was not significantly high, no tuning of the elastic properties was performed.

7. New Wing Design

A new wing structure was then idealized, based on the existing one. The foam core of the D-box was removed, and the overall number of ribs reduced, so as to reduce the overall weight of the structure. In order to stiffen it, fiberglass composite reinforcement was considered to be added to all ribs. Those ribs are 3 mm thick, made out of balsa wood. A central hole with a 10 mm radius is made in the central panel ribs. This feature serves the purpose of allowing for the passage of wires from the actuators and solar panels, also contributing towards a reduction of the weight of each rib. This hole becomes smaller, with a 5 mm radius, for the last rib of the central panel and for the ribs of the outer panels, up until the second to last aileron rib.

A simple rectangular cross-section beam was used as the main spar, with a thickness of 6 mm and a height of 20 mm.

A carbon tube containing a hollow circular cross-section, with an outer diameter of 8 mm and inner diameter of 6 mm is added near the trailing edge, providing the structure with greater resistance to torsion.

The wing is still built to be divided into three panels, although the point where they are connected is different: a central panel, consisting of the non tapered portion of the wing, up to 1400 mm in the spanwise coordinate, the other two being the tapered sections in each half wing. The two smaller panels contain an independent spar, which connects to the central panel by means of a stronger rib, to which a connecting element is added to provide support for the outer panel spar and carbon tube.

An aileron with a structure similar to that of the complete wing, made entirely of balsa wood, was designed, and attached by means of hinges to a balsa beam connected to the ribs of the main wing.

A thin balsa wood cover is applied to the leading edge and tip of the trailing edge to allow for the application of the heat-shrink plastic cover without it wrinkling.

Figure 14 shows the complete structure.

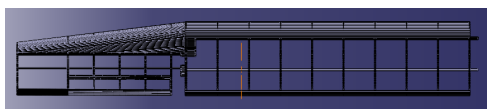


Figure 14: New wing design.

8. Wing Prototype Building Process

Due to the size of the complete wing, a half-scale model of a portion of the wing was built. The portion of the wing to be modeled was chosen to be from the root to the 1 m point along the spanwise direction. A model with a 0.5 m span is then obtained, containing a total of six ribs. A CAD model of that portion of the wing was obtained, and used as a guideline to the manufacture process.

The balsa beam and the carbon tube were obtained by cutting 1 m long specimens with the desired cross-section. After that, the ribs were hand-cut from 1.5 mm thick balsa sheets, and the circular holes in them created using a drill.

After cutting the ribs, the leading and trailing edge covers were produced. 1.5 mm thick balsa wood was also used. They were then bent to match the shape of the ribs. All parts were weighed at this point.

Fiberglass composite reinforcement was then added to the ribs and spar, and the weight change measured. A 55.67% increase in weight was registered for the spar, while the average rib weight increased 177.14%.

All parts were then assembled, using epoxy resin to glue them together, and the heat shrink plastic cover added. Table 10 shows a break-up of the weight of the several parts of the prototype presented in Figure 15.

Part	Weight[g]
Spar	6.32
Rib ($\times 6$)	0.97
Carbon tube	4.24
Leading edge cover (upper surface)	3.27
Leading edge cover (lower surface)	3.03
Trailing edge cover (upper surface)	1.21
Trailing edge cover (lower surface)	1.21
Heat-shrinking plastic	14.9
Epoxy used for assembly	1.37
Total	41.37

Table 10: Wing model break-up weights.

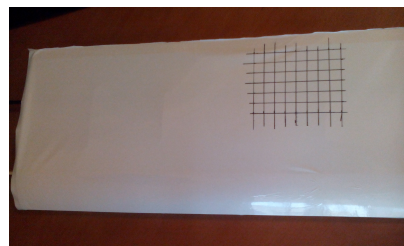


Figure 15: Heat-shrink film covered prototype.

9. Wing Prototype Testing

Having built the prototype, some experimental tests were performed, and the results compared to those yielded by a FEA using CATIA®.

9.1. Prototype Experimental Testing

Static tests were performed on the prototype before and after the heat-shrink cover was applied. The testing procedure was very similar to the one applied to the carbon tube, as seen in Figure 16. The span of the prototype after mounting it on the support was 416 mm.



Figure 16: Prototype testing.

A total of four loads were applied, and the displacement of the lower surface of the spar, directly below the point where the force was applied, was registered. This was done before and after applying the heat-shrink cover, and was concluded that that cover had little effect on the results. The results for both cases are presented in Table 11.

Load [gf]	Displacement (no cover) [mm]	Displacement (cover) [mm]
150	7.30	7.30
300	14.60	14.60
450	22.30	22.26
548	26.40	26.34

Table 11: Displacement of the bottom edge of the spar at the point where the force is applied.

9.2. Prototype Finite Element Analysis

The previously obtained CAD model of the prototype was adapted to match the experimental test conditions. The span was changed and only the portion of the model after the support was considered. Only the uncovered structure was considered, due to limitations identified in the software package.

Since a high number of elements was used in this analysis, given the amount of individual parts meshed, instead of quadratic tetrahedron elements, linear ones were used, to save computation time and obtain a finer mesh. Four different meshes were obtained, by tweaking the element size in each part of the assembly. In the thinner parts, such as the composite reinforcement of the ribs and the spar, a

smaller element size was used for all meshes. A convergence study was then carried out, considering an applied load of 4.41 N on the free end of the spar, acting in the vertical direction. It was seen that the maximum displacement was converging to 24.6 mm, with a 1626517 elements mesh. That mesh was chosen to perform the remaining analyses.

The maximum displacement of the spar was then found for all applied loads. Table 12 shows the values obtained for the displacement, as well as the relative difference to the experimental results. These discrepancies are relatively uniform regardless of the weight applied to the wing, averaging at 12%.

Load [gf]	Displacement [mm]	Relative difference
150	8.19	12.19%
300	16.40	12.33%
450	24.60	10.31%
548	29.90	13.26%

Table 12: Vertical displacement of the bottom edge of the spar at the point where the force is applied (FEA).

The Von-Mises stress distribution on the prototype was then checked. A maximum value of 96.5 MPa was obtained, in the upper surface of the carbon tube, near its clamped end. That value is significantly lower than the 1.65 GPa tensile strength suggested by most manufacturers, indicating that this part in particular is well within its elastic domain. It was also seen that the composite reinforcement layers near the root were the regions of the spar under a greater stress, of about 48 MPa, showing that they were fulfilling their mission and providing the structure with increased stiffness. Zooming in on the tip rib, the stress concentration near the edges where it connects to both the spar and the carbon tube was visible, and also near the trailing edge, where its surface area is lower and the cover is attached. The values of stress there were significantly lower than the ones identified previously in the carbon tube, in the order of 4.8 MPa, and were seen in the fiberglass reinforcement, as expected.

10. Conclusions

It was concluded that the experimentally determined values of the elastic properties of the materials used in the prototype were in accordance with tabulated values, and the numerical models obtained for each material were accurately predicting the results of the experimental tests.

Regarding the comparison between the experimental and FEA results for the tests of the prototype, it was concluded that the slight differences between the experimental prototype and the CAD model prevented the simulation from being more

accurate. These differences include inconsistencies rooting from the inherently inaccurate manual building process, which led to small differences in shape and wood fiber alignment in the ribs and eventual uneven thickness of the composite reinforcement. A certain degree of variation of the elastic properties between different specimens of balsa wood was also considered to be a source of error. Given all this factors, it was determined that if a more controlled building process, where the human factor is somewhat reduced, was adopted, it would result in parts with properties significantly more consistent, leading to a reduction in the uncertainty of the results of the FEA, when compared to those obtained experimentally.

Despite all these discrepancies, the relative differences were small enough to allow the numerical model to be considered valid for a preliminary design stage of the structure.

References

- [1] A. C. Marta and P. V. Gamboa. Long endurance electric uav for civilian surveillance missions. In *29th Congress of the International Council of the Aeronautical Sciences*, St. Petersburg, Russia, September 2014. ICAS.
- [2] Nuno M. A. Silva. Parametric Design, Aerodynamic Analysis and Optimization of a Solar Powered UAV. Master's thesis, Instituto Superior Técnico, 2014.
- [3] F. R. Menter. Improved two-equation k-omega turbulence models for aerodynamic flows. *NASA STI/Recon Technical Report N*, 93:22809, October 1992.
- [4] P. Malan, K. Suluksna, and E. Juntasaro. Calibrating the γ - re_θ transition model for commercial cfd. In *47th AIAA Aerospace Sciences Meeting*, St. Petersburg, Russia, October 2008. AIAA.
- [5] P. R. Spalart and S. R. Allmaras. A one-equation turbulence model for aerodynamic flows. *AIAA*, 1992.
- [6] Thomas C. Corke. *Design of Aircraft*. Pearson Education, Inc., 2003. ISBN:0130892343.
- [7] J. N. Reddy. *An Introduction to the Finite Element Method*. McGraw-Hill, 2006. ISBN:007-124473-5.
- [8] F. Beer, E. Johnston, J. Dewolf, and D. Mazurek. *Mechanics of Materials*. McGraw-Hill, 2012. ISBN:978-0-07-338028-5.
- [9] ASTM. D143-94 - Standard Test Methods for Small Clear Specimens of Timber. 1994.
- [10] Kretschmann, D. Mechanical Properties of Wood. Technical Report General Technical Report FPLGTR190, 1999.
- [11] ASTM. D3039 - Standard Test Method for Tensile Properties of Polymer Matrix Composite Materials. 2000.